Designed Synthesis of 3D Covalent Organic Frameworks

Hani M. El-Kaderi, *et al.*

Science **316**, 268 (2007);
DOI: 10.1126/science.1139915

Science (print ISSN 0036-8075; online ISSN 1095-9203) is published weekly, except the last week in December, by the American Association for the Advancement of Science, 1200 New York Avenue NW, Washington, DC 20005.

tional frequencies. In this degenerate scheme, the NR background has been addressed by means of the polarization-sensitive and interferometric techniques mentioned above.

A delayed probe has been used in time-resolved CARS (*19*–*22*). That technique uses ultrashort pulses for preparation and probing. Its ultimate source of species-specific information is multimode interference in the probe-delay signal profile, generally referred to as quantum beats (*19*). Time-resolved CARS eliminates the NR contribution by delaying the probe pulse, but the technique still remains vulnerable to fluctuations. It has been successfully applied to polycrystalline and opaque solids (*29*) to observe vibrational dephasing of single excited Raman transitions. However, the use of the multimode interference pattern for species recognition requires the ability to record high-quality quantum-beat profiles over a relatively large probe-delay span and therefore is challenging in the presence of scattering and fluctuations.

In our scheme, a generalized broadband or multiplex CARS technique is combined with background suppression by means of an optimal sequence of coherent excitation and time-delayed probe pulses. A schematic overview, pointing out the similarities and differences of the relevant established schemes and the one introduced here, is available online [figure S3 in (*24*)]. In short, we diverge from the conventional broadband CARS arrangement and deal with the probe and the two preparation pulses, pump and Stokes, separately. By adjusting the probe-pulse delay and its spectral width, we suppress the NR background, as in time-resolved CARS, but keep the advantages of the frequency-resolved multiplex CARS spectroscopy. The experimental data demonstrate the efficacy of the ultrafast broadband excitation and time-variable narrowband probing, whereas the described implementation supports the versatility of the technique.

References and Notes

1. P. R. Régnier, J. P.-E. Taran, *Appl. Phys. Lett.* **23**, 240 (1973).
2. J. W. Nibler, G. V. Knighten, in *Raman Spectroscopy of Gases and Liquids*, A. Weber, Ed. (Springer-Verlag, New York, 1979), pp. 253–299.
3. T. G. Spiro, *Biological Applications of Raman Spectroscopy* (Wiley, New York, 1987).
4. W. M. Tolles, R. D. Turner, *Appl. Spectrosc.* **31**, 96 (1977).
5. J. L. Oudar, R. W. Smith, Y. R. Shen, *Appl. Phys. Lett.* **34**, 758 (1979).
6. Y. Yacoby, R. Fitzgibbon, B. Lax, *J. Appl. Phys.* **51**, 3072 (1980).
7. E. O. Potma, C. L. Evans, X. S. Xie, *Opt. Lett.* **31**, 241 (2006).
8. D. Oron, N. Dudovich, D. Yelin, Y. Silberberg, *Phys. Rev. A.* **65**, 043408 (2002).
9. D. Oron, N. Dudovich, D. Yelin, Y. Silberberg, *Phys. Rev. Lett.* **88**, 063004 (2002).
10. S. H. Lim, A. G. Caster, S. R. Leone, *Phys. Rev. A.* **72**, 041803 (2005).
11. T. W. Kee, H. Zhao, M. T. Cicerone, *Opt. Express* **14**, 3631 (2006).
12. M. O. Scully *et al.*, *Proc. Natl. Acad. Sci. U.S.A.* **99**, 10994 (2002).
13. D. Klick, K. A. Marko, L. Rimai, *Appl. Opt.* **20**, 1178 (1981).
14. A. Voroshilov, C. Otto, J. Greve, *J. Chem. Phys.* **106**, 2589 (1997).
15. H. Kano, H. Hamaguchi, *Appl. Phys. Lett.* **85**, 4298 (2004).
16. G. I. Petrov, V. V. Yakovlev, *Opt. Express* **13**, 1299 (2005).
17. Y. R. Shen, *The Principles of Nonlinear Optics* (Wiley, New York, 1984).
18. H. A. Rinia, M. Bonn, M. Muller, *J. Phys. Chem. B* **110**, 4472 (2006).
19. R. Leonhardt, W. Holzapfel, W. Zinth, W. Kaiser, *Chem. Phys. Lett.* **133**, 373 (1987).
20. A. Materny *et al.*, *Appl. Phys. B* **71**, 299 (2000).
21. P. Beaud, H.-M. Frey, T. Lang, M. Motzkus, *Chem. Phys. Lett.* **344**, 407 (2001).
22. R. P. Lucht, S. Roy, T. R. Meyer, J. R. Gord, *Appl. Phys. Lett.* **89**, 251112 (2006).
23. P. Carmona, *Spectrochim. Acta A* **36**, 705 (1980).
24. The details of the experimental setup, a schematic overview of the established schemes (time-resolved CARS and multiplex/broadband CARS), and the technique introduced in this work are available as supporting material on *Science* Online.
25. A. P. Esposito *et al.*, *Appl. Spectrosc.* **57**, 868 (2003).
26. W. H. Nelson, R. Dasari, M. Feld, J. F. Sperry, *Appl. Spectrosc.* **58**, 1408 (2004).
27. M. D. Duncan, J. Reintjes, T. J. Manuccia, *Opt. Lett.* **7**, 350 (1982).
28. A. Zumbusch, G. R. Holton, X. S. Xie, *Phys. Rev. Lett.* **82**, 4142 (1999).
29. X. Wen, S. Chen, D. D. Dlott, *J. Opt. Soc. Am. B* **8**, 813 (1991).

30. We thank J. Laane and K. McCann for their generous assistance with spontaneous Raman measurements and gratefully acknowledge support from the Office of Naval Research (award N00014-03-1-0385), the Defense Advanced Research Projects Agency, NSF (grant PHY-0354897), an award from the Research Corporation, and the Robert A. Welch Foundation (grants A-1261 and A-1547).

Supporting Online Material

www.sciencemag.org/cgi/content/full/316/5822/268/DC1
Materials and Methods
Figs. S1 to S3
References

19 December 2006; accepted 26 February 2007
10.1126/science.1139055

Designed Synthesis of 3D Covalent Organic Frameworks

Hani M. El-Kaderi,[1] Joseph R. Hunt,[1] José L. Mendoza-Cortés,[1] Adrien P. Côté,[1] Robert E. Taylor,[1] Michael O'Keeffe,[2] Omar M. Yaghi[1]*

Three-dimensional covalent organic frameworks (3D COFs) were synthesized by targeting two nets based on triangular and tetrahedral nodes: ctn and bor. The respective 3D COFs were synthesized as crystalline solids by condensation reactions of tetrahedral *tetra*(4-dihydroxyborylphenyl) methane or *tetra*(4-dihydroxyborylphenyl)silane and by co-condensation of triangular 2,3,6,7,10,11-hexahydroxytriphenylene. Because these materials are entirely constructed from strong covalent bonds (C-C, C-O, C-B, and B-O), they have high thermal stabilities (400° to 500°C), and they also have high surface areas (3472 and 4210 square meters per gram for COF-102 and COF-103, respectively) and extremely low densities (0.17 grams per cubic centimeter).

The chemistry of linking organic molecules together by means of covalent bonds to isolate crystals of discrete zero-dimensional (0D) molecules and 1D chains (polymers) is well established; however, it is undeveloped for 2D and 3D COFs (*1*). COF structures that contain light elements (B, C, N, and O) should be able to combine the thermodynamic strength of covalent bonds, as those found in diamonds and boron carbides, with the functionality of organic units. Progress in this area has been impeded by long-standing practical and conceptual challenges. First, unlike 0D and 1D systems, the insolubility of 2D and 3D structures precludes the use of stepwise synthesis and makes their isolation in crystalline form very difficult. Second, the number of possible structures that may result from linking specific building-unit geometries into 2D or 3D extended structures is essentially infinite and complicates their synthesis by design.

We recently illustrated how the first challenge could be overcome by judiciously choosing building blocks and using reversible condensation reactions to crystallize 2D COFs in which organic building blocks are linked entirely by strong covalent bonds (*2*). Here we report how the design principles of reticular chemistry overcome the second challenge (*3*): Two nets based on the linking of triangular and tetrahedral shapes were selected and targeted for the synthesis of four 3D COFs.

Self-condensation and co-condensation reactions of the rigid molecular building blocks, the tetrahedral *tetra*(4-dihydroxyborylphenyl)methane (TBPM), and its silane analog (TBPS), and triangular hexahydroxytriphenylene (HHTP) (Fig. 1, A to C) provided crystalline 3D COFs (termed COF-102, COF-103, COF-105, and COF-108). These COFs are the most porous among organic materials, and a member of this series (COF-108) has the lowest density reported of any crystalline material. Without our a priori

[1]Center for Reticular Chemistry at California NanoSystems Institute, Department of Chemistry and Biochemistry, University of California, Los Angeles, 607 Charles E. Young Drive East, Los Angeles, CA 90095, USA. [2]Department of Chemistry and Biochemistry, Arizona State University, Tempe, AZ 85287, USA.

*To whom correspondence should be addressed. E-mail: yaghi@chem.ucla.edu

knowledge of the expected underlying nets of these COFs, their synthesis by design and the solution of their structures from powder x-ray diffraction (PXRD) data would have been prohibitively difficult.

In planning the synthesis, we chose the tetrahedral building blocks (Fig. 1, A and B) and the triangular unit (Fig. 1C), because they are rigid and unlikely to deform during the assembly reaction. Dehydration reactions of these units produce triangular B_3O_3 rings and C_2O_2B rings (Fig. 1, D and E). Based on these building blocks, we envisioned two kinds of reactions in which either of the tetrahedral blocks (Fig. 1, A and B) undergoes self-condensation or co-condensation with the triangular unit (Fig. 1C) to give COF structures based on nets with both tetrahedral and triangular nodes (Fig. 1, D and E).

In principle, there are an infinite number of possible nets that may result from linking tetrahedra with triangles. However, our analysis of previous assembly reactions suggests that the most symmetric nets are the most likely to result in an unbiased system and that those with just one kind of link will be preferred and are thus the best to target (*3*). In the present case of linking tetrahedral and triangular building blocks, the only known nets meeting the above criteria are those with symbols **ctn** and **bor** (Fig. 1, F and G) (*4*). The nodes of the nets are thus replaced by the molecular building units with tetrahedral and triangular shapes (Fig. 1, H and I). The use of rigid, planar triangular units, such as B_3O_3 rings, requires that rotational freedom exist at the tetrahedral nodes for the 3D structures **ctn** and **bor** to form.

We then used Cerius[2] software to draw the "blueprints" for synthesis of COFs based on **ctn** and **bor** nets by fitting molecular building blocks (Fig. 1, A and B) on the tetrahedral nodes and by fitting the triangular unit and the B_3O_3 ring (Fig. 1, C and D) on the triangular nodes of these nets adhering to their respective cubic space group symmetries: $I\bar{4}3d$ (**ctn**) and $P\bar{4}3m$ (**bor**). Energy minimization by means of force-field calculations was performed to produce the models in which all bond lengths and angles were found to have chemically reasonable values (*5*).

Synthesis of the COFs was carried out by suspending either TBPM or TBPS in mesitylene/dioxane. The suspensions were placed in partially evacuated (150 mtorr) Pyrex tubes, which were sealed and heated (85°C) for 4 days to give white crystalline COF-102 and COF-103 in 63 and 73% yields, respectively. Similarly, co-condensation of TBPM or TBPS with HHTP (3:4 molar ratio) produced green crystalline solids of COF-105 (58% yield) and COF-108 (55% yield) (*6*). The colors of COF-105 and COF-108 likely arise from the possible inclusion of a small amount of highly colored oxidized HHTP in their pores. The use of dioxane and mesitylene in their respective ratios was necessary to control the solubility of the starting materials and to maximize crystallinity of the products.

To show that the products of synthesis are indeed covalently linked into the designed structures, we studied the materials by PXRD, spectroscopy, microscopy, elemental microanalysis, and gas adsorption (*6*). A comparison of PXRD patterns of modeled COFs to those observed for the products of synthesis (Fig. 2, A to D) reveals that they are indeed the expected COFs with **ctn** or **bor** type. The observed PXRD patterns display narrow line widths and low signal-to-noise ratios indicative of the high crystallinity of COFs. A marked degree of correspondence between peak positions and intensities is also observed, substantiating that the H, B, C, and O atomic composition and positions in the respective modeled unit cells are correct. The PXRD data of the COFs could also be indexed, yielding unit cell parameters nearly identical to those calculated from Cerius[2] (table S5).

To further verify the unit cell parameters, PXRD patterns were subjected to model-biased Le Bail full pattern decomposition to extract the structure factor amplitudes from the x-ray data. For this procedure to be successful and yield acceptable reliability factors, a close correspondence in peak position and intensity between the model and the experimental data is required. All

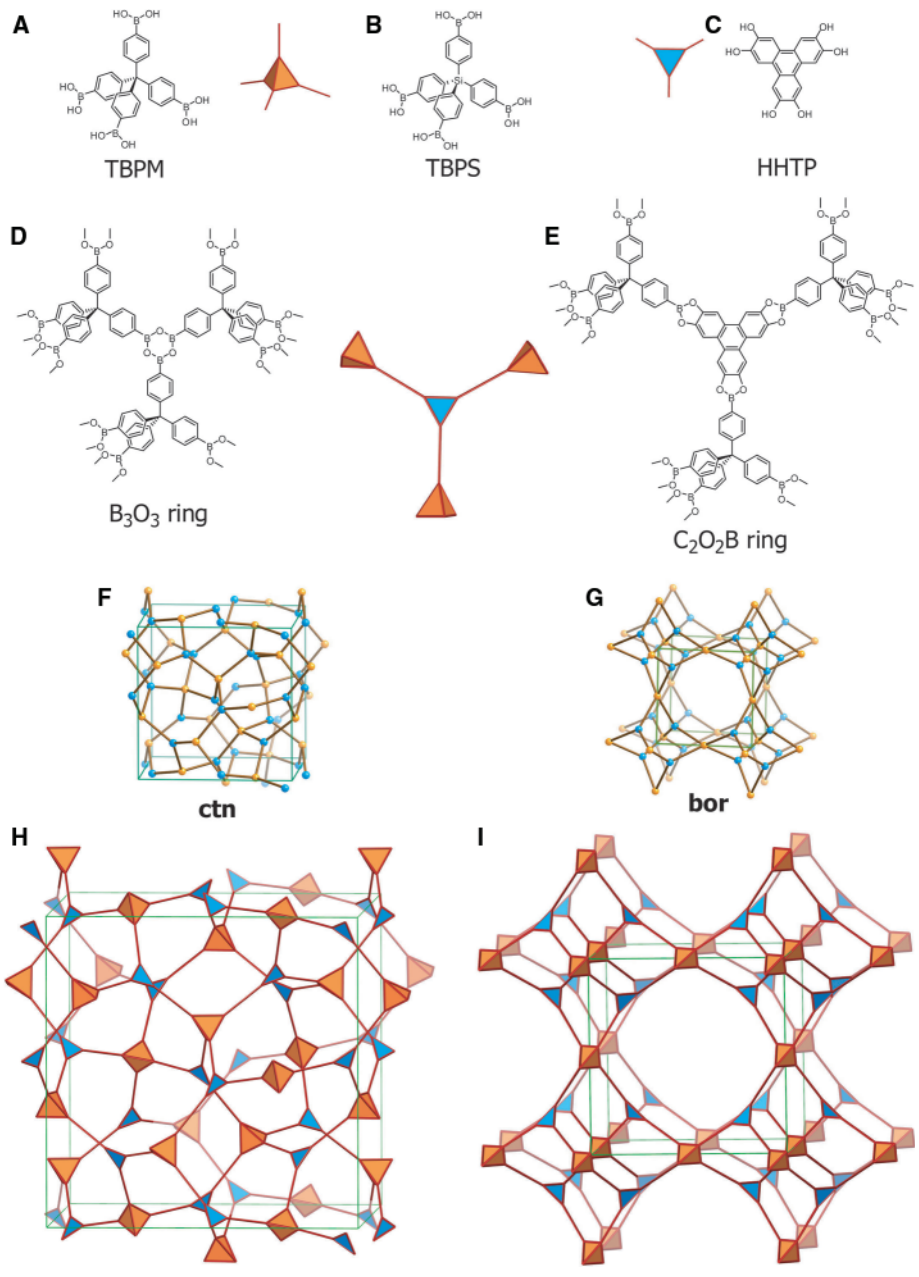

Fig. 1. Representative condensation routes to 3D COFs. Boronic acids are shown as tetrahedral building units [(**A**) and (**B**)], and a planar triangular unit (**C**) is also shown (polyhedron in orange and triangle in blue, respectively), including fragments revealing the B_3O_3 (**D**) and the C_2O_2B (**E**) ring connectivity in the expected linked products. These building units can be placed on the **ctn** (**F**) and **bor** (**G**) nets, as shown in the corresponding expanded nets (**H**) and (**I**), respectively.

peaks undergo some broadening because COF crystallites have micrometer dimensions (*7*). After accounting for line broadening in the initial stages of Le Bail extractions, fitting of the experimental profiles readily converged with refinement of the unit cell parameter, *a*. Refinements for all structures led, again, to values nearly identical to those calculated from Cerius[2] (table S5). Too few peaks were available to perform full Rietveld refinement of atomic positions and thermal parameters. Nonetheless, a near equivalence and low uncertainty [estimated SD (table S5)] between calculated and refined cell parameters, in addition to the facile and proper fit of the refined profiles [as indicated by statistically acceptable residual factors (table S6)], support the assertion that the COF structures are indeed those identified through modeling (Fig. 2; atomic coordinates in tables S1 to S4).

The covalent linking of building blocks through expected six-membered B_3O_3 boroxine

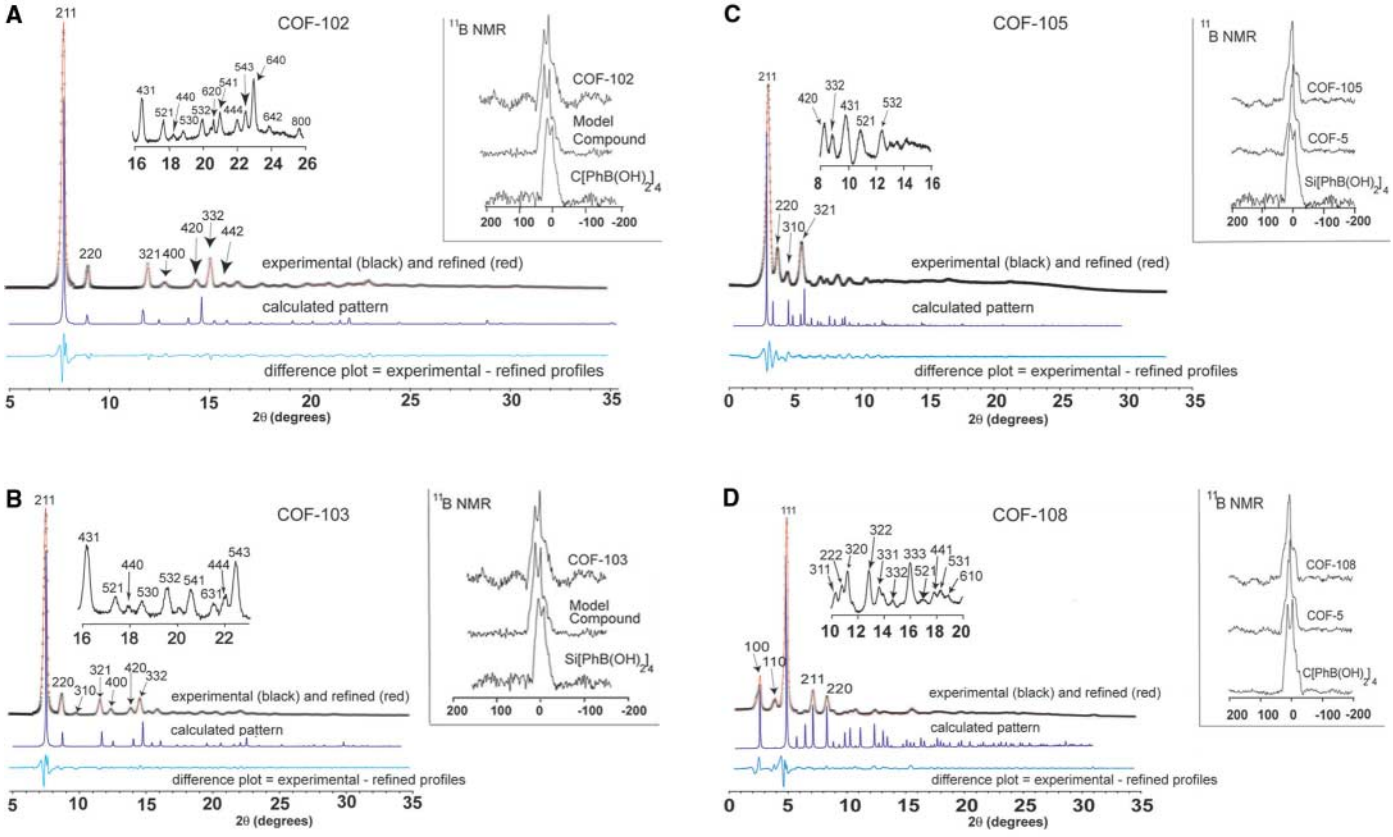

Fig. 2. Observed (experimental) and refined PXRD profiles for evacuated samples of COF-102 (**A**), COF-103 (**B**), COF-105 (**C**), and COF-108 (**D**), including patterns calculated with the use of Cerius[2], with observed profiles in black, refined profiles in red, calculated patterns in blue, and the difference plot (observed minus refined profiles) in turquoise. 2θ, Bragg angle in degrees. (Left insets) Expansion of observed PXRD profiles. (Right insets) ^{11}B MQ MAS NMR spectra (in parts per million) of COF (top trace), model compound (middle trace), and boronic acid (bottom trace) used to construct the corresponding COF.

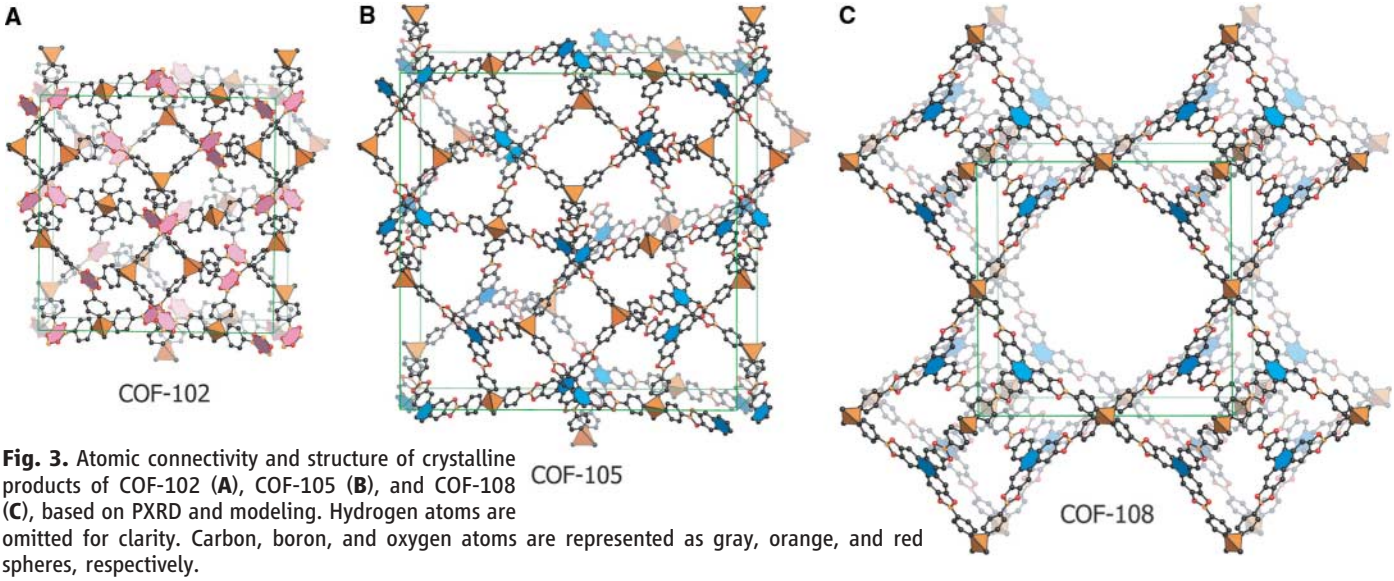

Fig. 3. Atomic connectivity and structure of crystalline products of COF-102 (**A**), COF-105 (**B**), and COF-108 (**C**), based on PXRD and modeling. Hydrogen atoms are omitted for clarity. Carbon, boron, and oxygen atoms are represented as gray, orange, and red spheres, respectively.

or five-membered C_2O_2B boronate ester rings in the COFs was assessed with Fourier transform infrared (FTIR) and multiple-quantum magic angle spinning nuclear magnetic resonance (MQ MAS NMR) spectroscopies. FTIR spectra of all COFs contain strongly attenuated bands arising from boronic acid hydroxyl groups indicative of successful condensation of the reactants (figs. S14 to S17). COFs prepared from self-condensation reactions all exhibit the diagnostic band at 710 cm^{-1} for the out-of-plane deformation mode of boroxine rings. Co-condensed COF-105 and COF-108 products have strong C-O stretching bands at 1245 cm^{-1} (COF-105) and 1253 cm^{-1} (COF-108), signals that are distinctive for boronate ester five-membered rings (*6*).

These FTIR spectroscopy data are fingerprints for the expected boron-containing rings; however, solid-state ^{11}B MQ MAS NMR spectroscopy is highly sensitive to the immediate bonding environment of boron. Any differences in B-C and B-O distances and/or angles will result in a notable change in the line shape and intensity of the spectra. The acquired ^{11}B MQ MAS NMR spectra for evacuated COFs were compared to those of molecular model compounds and starting materials (Fig. 2, A to D, right insets). The spectra of all of the COFs are coincident to those of the model compounds and are different from the starting materials. Thus, the boron-containing units in all the COFs have not only formed but are well-formed B_3O_3 and C_2O_2B rings. Additionally, data from ^{13}C and ^{29}Si MQ MAS NMR experiments show the presence of the expected number and environment of each type of respective nucleus, further substantiating the structural assignments (figs. S18 to S38).

In order to establish the phase purity and synthetic reproducibility of the COF materials, multiple samples were exhaustively imaged with scanning electron microscopy (SEM). The SEM images of COF-102 and COF-103 revealed agglomerated and nonagglomerated 1- to 2-μm-diameter spheres, respectively (figs. S39 and S40). This morphology is likely caused by a polar hydroxylated (-OH) surface that causes spherical crystal growth to minimize interfacial surface energy with the relatively nonpolar solvent media. The SEM images recorded for COF-105 and COF-108 revealed 5-μm platelets and 3- to 4-μm irregular spheres, respectively (figs. S41 and S42). For each of the COFs, only one morphology was observed, negating the presence of impurity phases. Furthermore, C and H elemental microanalysis confirmed that the composition of each COF corresponded to formulations predicted from modeling (*6*).

The derived structures for COF-102, COF-105, and COF-108 are shown in Fig. 3 (COF-103 has a tetrahedral Si replacing C, and its structure is virtually identical to that of COF-102). COF-102 (Fig. 3A), COF-103, and COF-105 (Fig. 3B) are based on **ctn**, and COF-108 (Fig. 3C) is based on **bor**. It is hard to assess why one of the two structure types would be preferred over the other. However, it is a notable confirmation of our original thesis that we find one or the other of the two structures. The only notable differences between the two structure types are that **bor** is about 15% less dense than **ctn** (compare the densities of COF-105 and COF-108) and has larger pores. The three-coordinated vertices in both structures are constrained to be planar with threefold symmetry, but the point symmetry at the tetrahedral site in **ctn** is only a subgroup ($\bar{4} = S_4$) of that at the tetrahedral site in **bor** ($\bar{4}m2 = D_{2d}$); this difference gives **ctn** less constraints and potentially makes it a more strain-free structure than **bor**.

It is also of interest to consider the pore sizes. In the COFs with the **ctn** structure, the center of the largest cavity in COF-102, COF-103, and COF-105 is 5.66, 5.98, and 10.37 Å, respectively, from the nearest atoms (H). If we allow for a van der Waals radius of 1.2 Å for H, spheres of diameter 8.9, 9.6, and 18.3 Å, respectively, are available in these three COFs. However, the pores in these materials are far from spherical, and we expect the effective pore size to be somewhat larger. COF-108 has two cavities, and the atoms closest to the center are C atoms at 9.34 and 15.46 Å. If we allow for a van der Waals radius of 1.7 Å for C, these cavities can accommodate spheres of 15.2 and 29.6 Å, respectively. It may be seen that the larger pores are well above the lower limit (20 Å) for the material to be described as mesoporous, and COF-108 is a rare example of a fully crystalline mesoporous material.

An important feature of 3D COFs is the full accessibility from within the pores to all the edges and faces of the molecular units used to construct the framework. A previous study found that maximizing the number of edges arising from aromatic rings in a porous material increases the number of adsorption sites and surface area (*8*). Porous zeolites, carbons, and metal-organic frameworks (MOFs) all contain latent edges in their structures; however, the structures of COFs contain no latent edges, and the entire framework is a surface replete with binding sites for gas adsorption. The structures also have extraordinarily low densities: COF-102 (0.41 g cm^{-3}), COF-103 (0.38 g cm^{-3}), COF-105 (0.18 g cm^{-3}), and COF-108 (0.17 g cm^{-3}). The last two values are markedly lower than those of highly porous MOFs such as MOF-5 (0.59 g cm^{-3}) (*9*) and MOF-177 (0.42 g cm^{-3}) (*8*) and are the lowest density crystals known (*10*) [compare these values with the density of diamonds (3.50 g cm^{-3})].

The low densities coupled with the maximized fraction of surface sites in 3D COFs naturally impart their exceptional porosities, which were shown in gas adsorption studies on evacuated samples of COF-102 and COF-103. Samples of "as synthesized" COF-102 and COF-103 were immersed in anhydrous tetrahydrofuran to remove solvent and starting materials

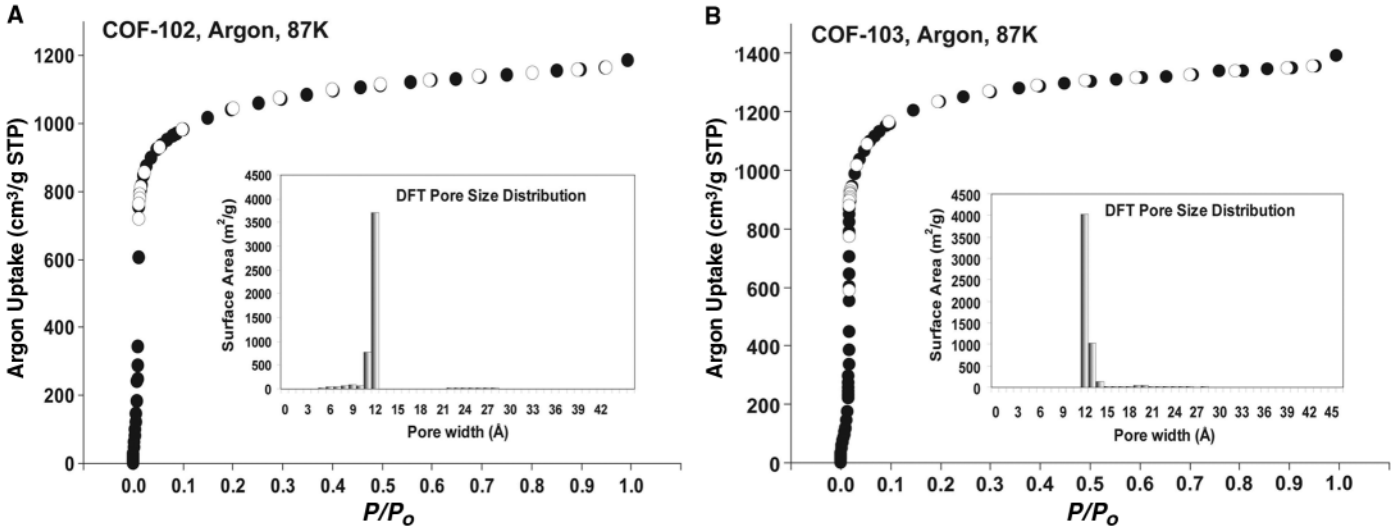

Fig. 4. Argon gas adsorption isotherms for COF-102 (**A**) and COF-103 (**B**) measured at 87 K and pore size histograms (insets) calculated after fitting DFT models to gas adsorption data. STP, standard temperature and pressure.

included in the pores during synthesis and were then placed under dynamic vacuum conditions (10^{-5} torr) for 12 hours at 60°C to completely evacuate the pores (*6*). Thermogravimetric analysis confirmed that all of the guests were removed from the pores and revealed the thermal stability of all COFs beyond 450°C (figs. S43 and S46). Argon isotherms for COF-102 and COF-103 were recorded at 87 K from 0 to 760 torr (Fig. 4, A and B). COF-102 and COF-103 exhibit a classic type I isotherm characterized by a sharp uptake at the low-pressure region between $P/P_o = 1 \times 10^{-5}$ to 1×10^{-2}, where P is gas pressure and P_o is saturation pressure. The apparent surface areas calculated from the Brunauer-Emmett-Teller (BET) model were 3472 and 4210 $m^2\ g^{-1}$ for COF-102 and COF-103, respectively. The pore volume determined from the Dubinin-Radushkevich equation afforded values of 1.35 $cm^3\ g^{-1}$ (COF-102) and 1.66 $cm^3\ g^{-1}$ (COF-103). The BET surface areas of COFs exceed porous carbons (2400 $m^2\ g^{-1}$) (*11*), silicates (1300 $m^2\ g^{-1}$) (*12*), recently reported 2D COFs (1590 $m^2\ g^{-1}$) (*2*), polymers of intrinsic microporosity (1064 $m^2\ g^{-1}$) (*13*), and polymer resins (2090 $m^2\ g^{-1}$) (*14*) and are comparable to some of the highest surface areas of MOFs [MOF-177 (4500 $m^2\ g^{-1}$) (*8*) and MIL-101 (4100 $m^2\ g^{-1}$) (*15*) (MIL, Matérial Institut Lavoisier)]. Calculation of pore size obtained from appropriately fitting density functional theory (DFT) models to the isotherms (figs. S48 and S52) yielded pore size distributions of COF-102 (11.5 Å) (Fig. 4A, inset) and COF-103 (12.5 Å) (Fig. 4B, inset) (*16*). Narrow distributions are obtained and are centered at values close to the pore diameters obtained from the crystal structures.

At the outset of this study, crystallization of 3D COFs (such as cross-linked polymers) was believed to be difficult, if not impossible, to achieve for both thermodynamic and kinetic reasons. This report demonstrates that this challenge can be met by striking a balance between these two competing factors and that the principles of reticular chemistry provide the basis for design and structure solution of the resulting materials.

References and Notes

1. *N* dimensional refers to materials indefinitely extended in *N* independent directions.
2. A. P. Côté *et al.*, *Science* **310**, 1166 (2005).
3. Reticular chemistry is concerned with the linking of molecular building blocks into predetermined structures by strong bonds (*17*).
4. O. Delgado-Friedrichs, M. O'Keeffe, O. M. Yaghi, *Acta Crystallogr. A* **62**, 350 (2006).
5. Cerius^2 Modeling Environment, version 4.2, Molecular Simulations Incorporated, San Diego, CA (1999).
6. A full description of the synthesis, characterization, and gas adsorption measurements can be found in the supporting material on *Science* Online.
7. B. D. Cullity, *Elements of X-ray Diffraction* (Addison-Wesley, Don Mills, Ontario, ed. 2, 1978).
8. H. K. Chae *et al.*, *Nature* **427**, 523 (2004).
9. H. Li, M. Eddaoudi, M. O'Keeffe, O. M. Yaghi, *Nature* **402**, 276 (1999).
10. The Cambridge Structural Database reports two structures with densities less than 0.18 g cm^{-3}. However, these reports arise from data deposited for incomplete structures where all atoms have not been included in the calculation of density.
11. N. Texier-Mandoki *et al.*, *Carbon* **42**, 2744 (2004).
12. M. Thommes, in *Nanoporous Materials Science and Engineering*, G. Q. Lu, X. S. Zhao, Eds. (Imperial College Press, London, 2004).
13. B. S. Ghanem *et al.*, *Chem. Commun.* **2007**, 67 (2007).
14. J.-H. Ahn *et al.*, *Macromolecules* **39**, 627 (2006).
15. G. Férey *et al.*, *Science* **309**, 2040 (2005).
16. K. Schumacher, P. I. Ravikovitch, A. D. Chesne, A. V. Neimark, K. K. Unger, *Langmuir* **16**, 4648 (2000).
17. O. M. Yaghi *et al.*, *Nature* **423**, 705 (2003).

18. The work was supported by Badische Anilin und Soda Fabrik (BASF) Ludwigshafen for synthesis, U.S. Department of Energy (DEFG0206ER15813) for adsorption, and NSF (DMR 0242630) for simulated structures. We thank H. Furukawa (Yaghi group) for invaluable assistance with porosity measurements. Crystallographic information files for COF-102, COF-103, COF-105, and COF-108 have been deposited into the Cambridge Crystallographic Data Centre (CCDC) under deposition numbers CCDC 637175 to 637178.

Supporting Online Material

www.sciencemag.org/cgi/content/full/316/5822/268/DC1
Materials and Methods
Figs. S1 to S56
Tables S1 to S6
References

16 January 2007; accepted 22 February 2007
10.1126/science.1139915

Direct Detection of the Asteroidal YORP Effect

Stephen C. Lowry,[1]* Alan Fitzsimmons,[1] Petr Pravec,[2] David Vokrouhlický,[3] Hermann Boehnhardt,[4] Patrick A. Taylor,[5] Jean-Luc Margot,[5] Adrian Galád,[6] Mike Irwin,[7] Jonathan Irwin,[7] Peter Kusnirák [2]

The Yarkovsky-O'Keefe-Radzievskii-Paddack (YORP) effect is believed to alter the spin states of small bodies in the solar system. However, evidence for the effect has so far been indirect. We report precise optical photometric observations of a small near-Earth asteroid, (54509) 2000 PH5, acquired over 4 years. We found that the asteroid has been continuously increasing its rotation rate ω over this period by $d\omega/dt = 2.0\ (\pm 0.2) \times 10^{-4}$ degrees per day squared. We simulated the asteroid's close Earth approaches from 2001 to 2005, showing that gravitational torques cannot explain the observed spin rate increase. Dynamical simulations suggest that 2000 PH5 may reach a rotation period of ~20 seconds toward the end of its expected lifetime.

The Yarkovsky-O'Keefe-Radzievskii-Paddack (YORP) effect is a torque that can modify the rotation rates and obliquities of small bodies in the solar system; its causes are incident solar radiation pressure and the recoil effect from anistropic emission of thermal photons (*1*). Several effects indicate that such a torque, as yet undetected, acts upon the surfaces of asteroids and meteoroids, and the YORP effect is the only realistic mechanism in these cases. A clear example of a YORP-evolved system can be seen within the Koronis asteroid family, formed by the catastrophic collisional disruption of a large parent body at least 2 billion years ago. This event would presumably have resulted in random spin states for the daughter asteroids, but surprisingly, the larger members are divided into two distinct alignments (*2*). Theoretical modeling invoked YORP as a potential mechanism to explain the spin-vector alignments by eventually altering the spin rates and obliquities, with some asteroids becoming trapped in spin-orbit resonances (*3*).

Another likely manifestation of YORP torques is the evolution of orbital semimajor axes of small members of asteroid families toward extreme values, which is important for determining their age (*4*). The evolving obliquity will have a direct bearing on the evolution of semimajor axes via Yarkovsky drift, a companion effect to YORP that is caused by a net force arising from emission of thermal radiation along the body's orbit and was recently detected for the first time (*5*). YORP is also an important component in models of the delivery of near-Earth asteroids from the main asteroid belt, as it leads to a Yarkovsky drift, forcing bodies into powerful perturbing orbital resonances (*6*).

Furthermore, there exists a distinct population of small, very-fast-spinning asteroids known as the monolithic fast rotators (MFRs) (*7*). If the orbits of such bodies are stable over million-year time scales, allowing YORP to significantly change the rotation rate, then the effect is highly

[1]School of Mathematics and Physics, Queen's University Belfast, Belfast BT7 1NN, UK. [2]Astronomical Institute, Academy of Sciences of the Czech Republic, Fricova 1, CZ-25165 Ondrejov, Czech Republic. [3]Institute of Astronomy, Charles University, V Holesovickách 2, 18000 Prague 8, Czech Republic. [4]Max-Planck-Institut für Sonnensystemforschung, Max-Planck-Strasse 2, 37191 Katlenburg-Lindau, Germany. [5]Department of Astronomy, Cornell University, Ithaca, NY 14853, USA. [6]Department of Astronomy, Physics of the Earth, and Meteorology, Faculty of Mathematics, Physics and Informatics, Comenius University, 842 48 Bratislava, Slovakia. [7]Institute of Astronomy, University of Cambridge, Madingley Road, Cambridge CB3 0HA, UK.

*To whom correspondence should be addressed. E-mail: s.c.lowry@qub.ac.uk